

Mars Aerobraking Spacecraft State Estimation By Processing Inertial Measurement Unit Data

Moriba K. Jah* and Michael E. Lisano II.†

Jet Propulsion Laboratory, California Institute of Technology, Pasadena, CA, 91040

George H. Born‡ and Penina Axelrad§

Colorado Center for Astroynamics Research (CCAR), University of Colorado, Boulder, CO, 80309

Aerobraking is an efficient technique for orbit adjustment of planetary spacecraft, such as Magellan (Venus), Mars Global Surveyor, and Mars Odyssey. Determination of the vehicle state during the aerobraking phase has conventionally been performed using only radiometric tracking data prior to and following the atmospheric drag pass. This approach is sufficiently accurate and timely to meet current mission operational requirements; however, it is expensive in terms of ground support and leads to delayed results because of the need for post-drag pass data. This research presents a new approach to estimation of the vehicle state during the atmospheric pass that sequentially incorporates observations from an Inertial Measurement Unit (IMU) and models of the vehicle and environment. The approach, called Inertial Measurements for Aerobraking Navigation (IMAN), is shown to perform at a level comparable to the conventional methods in terms of navigation accuracy and superior to them in terms of availability of the results immediately after completion of the pass. Furthermore, the research shows that IMAN can be used to reliably predict subsequent periapsis times and locations over all aerobraking regimes. IMAN also yields accurate peak dynamic pressure and heating rates, critical for a successful corridor control strategy, comparable to navigation team reconstructed values. This research also provides the first instance of the utilization of the Unscented Kalman Filter for the purpose of estimating an actual spacecraft trajectory arc about another planet.

Nomenclature

A_{tot}	= Spacecraft total projected area, m ²
C_d	= Drag coefficient
C_f	= Force coefficient
C	= Crosstrack
\bar{F}_{drag}	= Force due to drag
I	= Intrack, Identity
N	= Normal
NAV	= Navigation team
$\bar{\omega}$	= Spacecraft angular velocity vector, rad/s
$\bar{\omega}_{RWA}$	= Reaction wheel speed, rad/s
\dot{q}	= Heat rate, Watt/cm ²
q_{dp}	= Dynamic pressure, N/m ²
ρ	= Local density, kg/ m ³
R	= Radial
\mathbf{R}	= Rotation matrix

* Member Technical Staff, Guidance, Navigation, and Control Section, 4800 Oak Grove Dr., Pasadena, CA 91109.

† Technical Group Supervisor, Mission Analysis Software Engineering, 4800 Oak Grove Dr., Pasadena, CA 91109.

‡ Director CCAR and Professor, Aerospace Engineering Sciences, Campus Box 41, Boulder, CO 80301.

§ Professor and Associate Chair, Aerospace Engineering Sciences, Campus Box 41, Boulder, CO 80301.

σ	= Standard deviation
T	= Transverse
\bar{V}	= Local spacecraft relative velocity vector, m/s
V	= Velocity

I. Introduction

Aerobraking is a spaceflight technique that makes use of atmospheric drag to decrease the velocity of a spacecraft^{**}. This is coupled with a proportional decrease in the semi-major axis of the orbit. Initially, the vehicle is inserted into a highly eccentric orbit with periapsis located within the atmospheric influence of the planet. The spacecraft employing aerobraking is set to “fly” in a designed atmospheric corridor, historically based upon heat rate or dynamic pressure. Aerobraking is employed until the desired apoapsis altitude is achieved, at which time the spacecraft performs a propulsive periapsis-raising maneuver placing it in its final orbital configuration. The use of aerobraking for orbit adjustment reduces the required propellant and, consequently, both the spacecraft mass and mission cost.

Aerobraking introduces operational costs and risks; examples from flown missions to date include the following:

1. The spacecraft slews into a designed aerodynamically stable orientation prior to each drag pass. Traditionally, there is a loss of radiometric tracking precisely when the spacecraft “flies” through the most dynamically unknown portion of its trajectory^{††}. Due to the lack of tracking data, this results in a significant increase of the post-drag-pass spacecraft state^{‡‡} uncertainty.
2. The aerobraking orbit reconstruction process can be very time consuming (i.e., lasting several hours for each orbit) and workforce intensive (6 full-time-equivalent navigators for the 3 month Mars Odyssey 24/7 aerobraking operations). In contrast, nominal navigation operations consist of a traditional work week and workforce (2 to 3 navigators working 8 hour days, 5 days a week).
3. All of the spacecraft events occur on a ground-generated timeline via a sequence of commands that is uploaded to the spacecraft and is triggered by the on-board clock. In order for this sequence to be produced, the navigation team must receive post-drag pass radiometric data and deliver a predicted trajectory. Any delay in receiving post drag-pass radiometric data may compromise spacecraft safety as an updated sequence may not be generated for the subsequent pass. The spacecraft would then have to rely on a less accurate background sequence. Spacecraft events take place at times relative to the predicted time of periapsis. Significant errors in this prediction (> 225 seconds) could lead to:
4. Aerobraking corridor control maneuver errors and thus inefficient propellant usage.
5. Spacecraft attitude errors exceeding a 20 degree bandwidth at the time of control authority switch from reaction wheels to attitude control thruster system, capable of inducing inadvertent compensative thruster firings, and thus another source of inefficient propellant usage. Inadvertent safe-mode entry triggering is another possible outcome.

These costs and risks can be mitigated by making use of the information provided by Inertial Measurement Units (IMU) for navigation, augmenting current navigation capabilities and providing mission robustness. The IMU gyroscopes provide data on the rotational states of the spacecraft, while the accelerometers measure the effects of non-gravitational forces, such as those due to atmospheric drag (i.e., precisely the environment not captured by current radiometric tracking techniques as previously explained). This project demonstrates how to exploit this sensitivity for navigation performance, and thus reduce costs and risks.

Historical uses of IMUs for interplanetary spacecraft are deterministic (i.e. used in lieu of a dynamic model), and as a result do not statistically improve the knowledge of the spacecraft state. This research implements the IMU data as orbit determination measurements, providing post drag-pass spacecraft position and velocity estimates, realistic reconstructed atmospheric density profiles, and accurate subsequent periapsis time estimates, without the need to process post-drag pass radiometric data. In this way, it serves as an independent assessment of the drag-pass dynamics. It should be noted that the information provided by an IMU is strongly dependent on the initial conditions, since the IMU measurements are relative to the initial state of the spacecraft.

^{**} This method has been successfully implemented by Magellan (at Venus), Mars Global Surveyor, and Mars Odyssey.

^{††} This is due to conflicts between physical constraints in spacecraft design {such as possible articulation or fixed placement of antennas} and variable spacecraft-to-Earth geometry throughout aerobraking required for tracking.

^{‡‡} Throughout this paper, when the term “spacecraft state” is used, it refers to the spacecraft position and velocity.

The IMU-based spacecraft state estimates are achieved more rapidly than those achieved via the current method which requires the collection and reduction of post drag-pass radiometric data. Since Mars-bound spacecraft are already equipped with IMUs, making use of these measurements comes at no additional hardware expense to a flight project.

A. Historical Uses of IMU Data and Previous Research

The suggested use of IMU data as orbit determination measurements is not new^{1, 2}. In fact, it was suggested as early as 30 years ago³. However, the use of IMU data in this capacity was not implemented for various reasons. One main reason is that until recently, these instruments were too massive and required a significant amount of power to be included as a standard spacecraft payload. Current technology such as Multisensor Inertial Measurement Units [MIMU]) allows IMUs to be standard spacecraft payloads. Thus, with regards to hardware, making use of these data for navigation is monetarily transparent to any mission.

Typical uses for accelerometer data on interplanetary missions have been used to control and assess maneuvers^{§§}, orbit insertions, and atmospheric entries^{***}. Interplanetary maneuvers are either sequenced (i.e., preloaded and triggered off of the spacecraft clock) or autonomous (as is for some Angular Momentum Desaturation events). They are not commanded in real-time mainly due to radio signal light-time travel constraints. Because of this, IMUs are also used as thruster cutoff sensors by measuring the amount of applied thrust and triggering the shutoff upon reaching the designed thrust levels^{†††}. This is also applied for Trajectory Correction Maneuvers (TCMs) and aerobraking maneuvers (ABMs).

Earth based missions such as GRACE, use the accelerometer data as a means of measuring non-gravitational accelerations to subtract them from the dynamics in order to refine knowledge of the gravitational field of the Earth. IMU data collected during Space Shuttle operations has been used to characterize the rarefied flow regime encountered during reentry, and to formulate realistic aerodynamic coefficient tables⁴.

During EDL, the IMU output is used onboard in lieu of non-gravitational dynamic equations. This has been the case for both the Viking (1976) and Mars Pathfinder (1996) missions. There has been recent work in this area (EDL) seeking to incorporate IMU data as navigation measurements instead of the traditional use of the data directly into the computed dynamics^{‡‡‡, 5, 6}. For aerobraking, the IMU data has been used as a deterministic drag pass assessment tool. Ref. 7 developed a tool called Periapsis Timing Estimator (PTE). This tool takes the IMU data as truth, and returns an estimate of the drag pass change-in-velocity along with the time at which the centroid of the drag pass occurred. It uses this information to predict the subsequent periapsis time, based on an analytic equation relating change-in-velocity to change-in-orbit-period. This method does not filter the IMU data, nor does it integrate a trajectory. Rather, it compares several drag pass metrics with those predicted by the navigation team, and suggests corrections.

The ultimate goal of this research is to pave a road for future aerobraking missions, leading to the capability of onboard navigation. This ability would allow for the spacecraft to autonomously perform aerobraking corridor control maneuvers and drag-pass/Earth communication attitude slews, breaking away from current absolute ground operations dependency. In order to validate the approach of using the IMU data type for aerobraking navigation, two research routes were taken: the first was to process simulated IMU data, and the second was to process flight IMU data.

B. Overview of Research

Section II provides an overview of the navigation strategies common to the aerobraking phase of a mission. Pros and cons are presented along with current aerobraking navigation accuracy capabilities. Section III provides a description of an IMU, from concept to typical sources of error. The chapter also discusses kinetic IMU measurement sensitivities. Section IV provides results from processing flight data obtained from the 2001 Mars Odyssey orbiter mission. Finally, Section V provides a summary of this research, the conclusions, and makes recommendations for the direction of future work in this area.

§§ Trajectory Correction Maneuvers (TCMs) are an example.

*** Entry, Descent, and Landing (EDL) operations

††† Typically, there is a redundant shutoff system is based upon a thruster-on time (like an egg timer), and should the IMU fail, the thruster will shut off once the allotted time has expired.

‡‡‡ Bishop, R. (2001). Precision Entry Navigation Dead-Reckoning Error Analysis – Theoretical Foundations. Personal Notes, University of Texas at Austin, TX.

II. Current Aerobraking Operations and Strategies

To date^{§§§}, there have been three successful interplanetary aerobraking missions: Magellan at Venus^{8, 9}, Mars Global Surveyor¹⁰, and Mars Odyssey¹¹. The spacecraft employing aerobraking is set to “fly” in a designed atmospheric corridor. For Mars Odyssey, the performance index of choice is heat rate^{****} (in units of watts/cm²), which is defined by cf. Ref. 12 as:

$$\dot{q} = \frac{1}{2} \rho V^3 \quad (1)$$

where: ρ is the local density
 V is the inertial velocity of the s/c relative to the atmosphere.

The spacecraft can only tolerate a finite amount of heat for a given amount of time, making the heat rate a required corridor control parameter^{††††}. The heat rate and maximum temperature set the upper limit of the aerobraking corridor. There is usually a mapping orbit constraint driving the maximum duration that can be spent aerobraking; the lower limit is set such that the spacecraft can survive for a given amount of time without an orbit adjustment. For Mars Odyssey, this amount of time was 48 hours.

The spacecraft velocity is greatest at periapsis. Thus, predicting the periapsis altitude is directly related to the ability in predicting the spacecraft velocity magnitude at periapsis (since periapsis velocity is related to radial distance from the central body). Since the heat rate is a function of the spacecraft velocity, being able to predict this velocity is important. The main perturbing factor influencing periapsis altitude is the gravitational field. Therefore, modeling the gravity accurately is critical in order to minimize spacecraft state errors. When a high-density value is solved for following the drag pass, what must be successfully determined is whether the increase in density occurred due to a lower periapsis altitude, or an expanding atmosphere (as would be the case if a dust storm were taking place). A change in periapsis altitude due to gravity perturbations may be tolerated, but a maneuver would most likely have to be performed if a dust storm were encountered.

All of the spacecraft events occur on a timeline that is generated by ground personnel. These events take place at times relative to the predicted time of periapsis. Errors in this prediction map into aerobraking maneuver (ABM) errors (thruster gravity losses). ABMs are designed to occur in combination with specific spacecraft attitude configurations, mostly aligned with the velocity vector at apoapsis. Hence, a timing error would directly translate into an attitude error at the time of the burn, and thus the burn would be inefficient as compared to its design⁶. There were 32 ABMs performed over a 3 month span, on the Mars Odyssey mission.

During the drag pass, the spacecraft attitude is compared against a time varying attitude profile (since the spacecraft attitude changes by approximately 40 degrees over the entire drag pass arc). Outside of the atmosphere (in the vacuum phase of the orbit), the spacecraft attitude is fixed (with the exception of ABM attitudes) such that

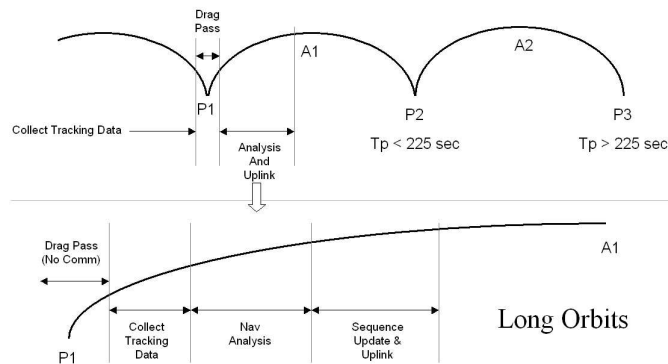


Figure 1. Long orbit period aerobraking navigation strategy. This plot was taken from a Mars Odyssey Navigation PowerPoint presentation by Robert Mase, 2002

§§§ The Mars Reconnaissance Orbiter mission is set to aerobrake from April 2006 to September 2006.

**** For Mars Global Surveyor and Magellan, this index was atmospheric dynamic pressure.

†††† The adhesive used on the solar panels sets the maximum temperature constraint that the spacecraft can experience at any given time. This maximum temperature is what drives the maximum heating rate or dynamic pressure.

the high gain antenna is pointed at Earth⁺⁺⁺⁺. The attitude control authority is typically given to the reaction wheel assembly (RWA), but for the drag pass it is switched to the attitude control system (ACS) thrusters. A 20 degree dead band is usually allotted for tolerable nominal attitude offset during the drag pass. Historically, this 20 degree offset from the nominal attitude is equivalent to a timing error of approximately 225 seconds. Therefore, the navigation team must be able to predict subsequent periapsis times to within this tolerance. Otherwise, propellant would be wasted due to the spacecraft thrusters fighting aerodynamic torques. Figure 1 illustrates a typical long orbit (~ 16 hour orbit period) aerobraking navigation operations plan.

The capability of the navigation team to predict subsequent periapsis times is dominated by the atmospheric density uncertainty. For example (Mars Odyssey), assume an uncertainty of 35% (1σ). For large orbit periods, the expected change in period due to drag could be 1000 seconds. With a 105% 3σ atmospheric density uncertainty, that means that the change in period could be off by 105%, in this case 1050 seconds. This clearly violates the 225 second timing error constraint. Therefore, for large orbit periods, the navigation team usually can not predict (with confidence) periapsis time to within the 225 second constraint, for more than one subsequent orbit as shown in Fig. 1. However, for the smaller orbits, where the expected period change could be as low as 30 seconds, with a 105% uncertainty, the navigation team can make predictions for many subsequent orbits¹³.

The current navigation operations plan for aerobraking requires 24 hours a day, 7 days a week staffing. Each drag pass is reconstructed, and there are daily meetings in order to make corridor control decisions (i.e., ABM scheduling). The orbit determination for aerobraking is as follows:

1. Obtain spacecraft initial conditions from the last solution (make epoch start at the beginning of tracking data received immediately following the previous drag pass).
2. Obtain post drag-pass attitude profile, atmosphere model inputs (baseline assumptions), and small forces data (i.e., RCS thruster firings).
3. Collect tracking data from epoch (beginning of radiometric data following the previous drag-pass) up to approximately 1.5 hours following the drag pass. This 1.5 hours accounts for the fact that tracking is not initiated until 30 minutes after periapsis and about 1 hour of Doppler is fit post drag-pass. This can be seen in Fig. 1.
4. Reconstruct the drag pass for the orbit(s) by means of a radiometric data least squares fit and save salient information (i.e., density, heat rate, etc).
5. Predict the trajectory of future orbits, using the atmospheric model of choice^{§§§§}.
6. Generate and deliver the Orbit Propagation and Timing Geometry (OPTG) and spacecraft ephemeris (SPK {Spice Kernel}) files to the appropriate servers/archival directories for use by science and engineering teams.

The deterministic future orbits prediction is compared to a design baseline and assessed with the corridor control strategy. The navigation team determines whether or not to implement an ABM. This entire process is very time consuming, and the staffing cost expensive. For the Mars Odyssey mission, the navigation team had 3 hours past periapsis time to receive data, fit it, and deliver an orbit solution. There were seven full-time-equivalent navigators^{*****} on the team for a 24/7 operations support. To place this in perspective, a nominal operations plan for interplanetary orbiters calls for regular 8 hour shifts during a normal work week, with only about three navigators at the most. This gives merit to the effort in developing or implementing a method that minimizes both computation time and workload, such as the one shown in this research.

⁺⁺⁺⁺ Mars Global Surveyor was spin stabilized during the vacuum phase of the aerobraking orbit.

^{§§§§} For Mars Odyssey, a version of the MarsGRAM atmosphere model was used. This model is produced by Jere Justus at the NASA Marshall Space Flight Center.

^{*****} Not all of them were full time equivalents.

III. Inertial Measurement Units

This chapter has the purpose of providing a brief and simple description of what an IMU is, the physical principles behind its operation, and common error sources. The examples provided here are not constrained to the IMUs that are carried by Mars-bound spacecraft. The description and examples provided are for a general understanding of the principles governing IMU sensors.

A. IMU Description

Generally, IMUs are comprised of accelerometers and gyroscopes. The accelerometer senses the specific contact force (rectilinear non-conservative acceleration) experienced by the IMU case, and the gyroscope senses angular deviations or rates (when differentiated) experienced by the case. Typically, the IMU is fixed to the spacecraft. This implies that the transformation between the IMU case frame and the spacecraft body frame is a constant matrix.

A simple accelerometer can be described as a proof mass, suspended within a case. If the spacecraft, and thus the case, are either at rest or experiencing a constant rectilinear motion, then the output of the accelerometer should be null. This is because the proof mass is also in equilibrium with the spacecraft. However, if an external force is applied to the case, the proof mass (due to its inertial properties) will experience an acceleration with respect to the case. It is this acceleration that the accelerometer will sense. This is why the accelerometer does not register gravitational accelerations⁺⁺⁺⁺.

Although the accelerometer senses acceleration, the output of the accelerometer is typically a current or a voltage. For instance, the accelerometers on Mars Odyssey have a seismically sensitive pendulous quartz structure that outputs an acceleration-proportional current¹⁴. In the case of an electromagnetically suspended proof mass, the amount of voltage required in order to keep the proof mass centered in the case is proportional to the acceleration experienced by the proof mass. Therefore, the acceleration can be inferred from the supplied voltage⁺⁺⁺⁺.

The gyroscope has three degrees of freedom, with each axis of each gimbal^{§§§§} equipped with a sensor (pickoff) which detects angular displacements. The amount of control torque required in order to null the pickoffs is used to compute the experienced angular rates. The gyroscopes used on Mars Odyssey are ring-laser-gyroscopes (RLG), which are a “strapdown” system.

For each accelerometer, there is a counter which keeps track of quantized changes in velocity experienced by the proof mass. These counts are monotonically increasing until they reach a specific threshold. At this threshold, the counter “rolls over” (similar to an odometer) and it is reinitialized. The quantities recorded in the telemetry are counts of change in velocity within the set sample time. In the case of Mars Odyssey, high-rate IMU data was sampled at 200 Hz.

⁺⁺⁺⁺ The proof mass is experiencing the same gravitational field simultaneously with the spacecraft itself (i.e., they are both in a state of freefall).

⁺⁺⁺⁺ Typically, the proof mass will have one degree of freedom, so as to isolate the acceleration experienced along a preferred axis (i.e., minimize cross-coupling effects).

^{§§§§} The difference between the platform and strapdown system is that the platform system has parts which move independently of the platform. Strapdown systems are “tied” to the platform or case and move with the case.

B. Common IMU Error Sources

For both accelerometers and gyroscopes, there are a number of error sources which corrupt the measurements; some of those are as follows¹⁴:

1. Bias
2. Scale Factor
3. Sensitivity
4. Non-linearity
5. Repeatability
6. Misalignment/Non-orthogonality
7. Noise

The bias can be defined as the instrument output with no input acceleration or rotational rate present. Bias is a signed quantity usually expressed in units of acceleration. Before and after each drag pass, the bias can be evaluated and subtracted off of the measured accelerations in a straightforward manner. There usually is a certain amount of drift in the bias, over the data collection period. However, it is relatively small and not difficult to determine or estimate. The bias stability (drift) is a function of temperature fluctuations^{*****}.

The scale factor is defined as the ratio of the change in output (in volts or amperes) to a unit change of the input (in units of acceleration). It is typically given in mA/g or V/g. The scale factor error is expressed as a percentage or in parts per million (of full scale). The scale factor is sensitive to the same factors as the bias.

The sensitivity can be defined as the ratio of a change in response to a change in an undesirable or secondary input (as the scale factor variation to a unit of power supply voltage change). Next, the non-linearity can be defined as the deviation of the accelerometer output from the input-output linear fit over the operating range. The deviation is expressed as a percentage of the full-scale output⁺⁺⁺⁺⁺. Finally, the repeatability concerns the closeness of agreement among measurements of the same variable, repeated under the same conditions, especially when changes in conditions occur or when operation is interrupted between the measurements. The misalignment describes errors in mounting of the sensor to the spacecraft frame and the non-orthogonality refers to the error in orthogonality between all input axes. Noise can be understood as undesired perturbations in the IMU output signal, which are generally uncorrelated with desired or anticipated input. Noise in the IMU output is of two types: intrinsic and seismic. Intrinsic noise is generated within the IMU and represents the limiting factor in making measurements. Intrinsic noise is random in nature and is characterized by a noise power spectral density (PSD) curve. Gyroscope noise is correlated (colored), and characterized by a random walk process. For MGS, the accelerometer had an intrinsic noise of approximately 8 μg . Seismic noise is a true input acceleration (usually unanticipated by the user). It results from noise sources in the local environment and their transmission to the IMU through the mounting structure that supports the IMU.

C. IMU Measurement Model

The model for the IMU (accelerometer and gyroscope⁺⁺⁺⁺⁺) is defined by cf. Ref. 6 as follows:

Let,

$\bar{a}_m^c \equiv$ measured acceleration in the IMU case frame

$\bar{\omega}_m \equiv$ measured angular velocity

$$\bar{a}_m^c = (I + \Lambda_a)(I + \Sigma_a)(\mathbf{T}_c^{ric} \bar{a}_{non-grav} + \mathbf{T}_c^{body} \bar{a}_{rotation} + \bar{b}_a + \bar{\epsilon}_a) \quad (2)$$

where

***** For Mars Global Surveyor, the accelerometer temperature variation did not exceed 0.234 degrees Celsius over the entire 201 aerobraking passes of Phase 1. This corresponded to a bias drift of approximately 1%¹⁵.

+++++ An optional representation is to provide non-linearity coefficients (i.e., K2 ($\mu\text{g}/\text{g}^2$) and K3 ($\mu\text{g}/\text{g}^3$))¹⁴.

+++++ Although the gyroscope data are not used as a state observation (in this research) but rather as a deterministic truth model, the gyroscope measurement model is derived for completeness.

$\mathbf{T}_c^{ric} \equiv$ transformation matrix from radial-intrack-crosstrack to the case frame

$\mathbf{T}_c^{body} \equiv$ transformation matrix from the body frame to the case frame

$\Lambda_a \equiv$ accelerometer misalignment/non-orthogonality errors (in the case frame)

To better describe Eqn. 2, let

$$\begin{aligned} a_{misalignme \quad nt-X} &= a_x \hat{x} + a_y \gamma_{xz} \hat{y} - a_z \gamma_{xy} \hat{z} \\ a_{misalignment-Y} &= -a_x \gamma_{yz} \hat{x} + a_y \hat{y} + a_z \gamma_{yx} \hat{z} \\ a_{misalignment-Z} &= a_x \gamma_{zy} \hat{x} - a_y \gamma_{zx} \hat{y} + a_z \hat{z} \end{aligned} \quad (3)$$

Thus,

$$\begin{bmatrix} a_{misalignment-X} \\ a_{misalignment-Y} \\ a_{misalignment-Z} \end{bmatrix} = \left\{ \begin{bmatrix} 1 & & \\ & 1 & \\ & & 1 \end{bmatrix} + \begin{bmatrix} 0 & \gamma_{xz} & -\gamma_{xy} \\ -\gamma_{yz} & 0 & \gamma_{yx} \\ \gamma_{zy} & -\gamma_{zx} & 0 \end{bmatrix} \right\} \begin{bmatrix} a_x \\ a_y \\ a_z \end{bmatrix} \quad (4)$$

So,

$$\Lambda_a = \begin{bmatrix} 0 & \gamma_{xz} & -\gamma_{xy} \\ -\gamma_{yz} & 0 & \gamma_{yx} \\ \gamma_{zy} & -\gamma_{zx} & 0 \end{bmatrix} \quad (5)$$

$\Sigma_a \equiv$ accelerometer scale factor errors (in the case frame)

$$\Sigma_a = \begin{bmatrix} \sigma_x & 0 & 0 \\ 0 & \sigma_y & 0 \\ 0 & 0 & \sigma_z \end{bmatrix} \quad (6)$$

$\bar{b}_a \equiv$ accelerometer bias (in the case frame)

$\bar{\mathcal{E}}_a \equiv$ accelerometer noise (white)

$$E[\bar{\mathcal{E}}_a] = 0$$

$$E[\bar{\mathcal{E}}_a(t) \bar{\mathcal{E}}_a^T(\tau)] = \bar{R}_a(t) \delta(t - \tau) \quad (7)$$

Assuming that the misalignment and scale factor errors are relatively small, then to first order we can say that:

$$(I + \Lambda_a)(I + \Sigma_a) \approx I + \Lambda_a + \Sigma_a = I + \Delta_a \quad (8)$$

where

$$\Delta_a = \Lambda_a + \Sigma_a$$

Then,

$$\bar{a}_m^c = (I + \Delta_a) (\mathbf{T}_c^{ric} \bar{a}_{non-grav} + \mathbf{T}_c^{body} \bar{a}_{rotation} + \bar{b}_a + \bar{\varepsilon}_a) \quad (9)$$

Therefore, in order to get the observed accelerations due to aerodynamic effects

$$\bar{a}_{non-grav\ observed} = \mathbf{T}_{ric}^c \left[(I + \Delta_a)^{-1} \bar{a}_m^c - (\mathbf{T}_c^{body} \bar{a}_{rotation} + \bar{b}_a + \bar{\varepsilon}_a) \right] \quad (10)$$

where

$\mathbf{T}_{ric}^c \equiv$ transformation matrix from the case frame to radial-intrack-crosstrack

A similar formulation can be made for the gyroscope, thus let

$$\bar{\omega}_m = (I + \delta_g) (I + \Gamma_g) (\bar{\omega}_{true} + \bar{b}_g + \bar{\varepsilon}_g) \quad (11)$$

where

$\delta_g \equiv$ gyro misalignment/non-orthogonality errors

$$\delta_g = \begin{bmatrix} 0 & \delta_{gxz} & -\delta_{gxy} \\ -\delta_{gyz} & 0 & \delta_{gyx} \\ \delta_{gzy} & -\delta_{gzx} & 0 \end{bmatrix} \quad (12)$$

$\Gamma_g \equiv$ gyro scale factor errors

$$\Gamma_g = \begin{bmatrix} \nu_{gx} & 0 & 0 \\ 0 & \nu_{gy} & 0 \\ 0 & 0 & \nu_{gz} \end{bmatrix} \quad (13)$$

$\bar{b}_g \equiv$ gyro bias

IV. Results From Mars Odyssey Aerobraking

IMU data was first fit based on simulated scenarios. Once the simulated scenario produced acceptable results, the next step was to ascertain whether or not flight data could be successfully processed. The Odyssey orbiter performed three months of aerobraking, beginning with a 19 hour orbit and aerobraking down to a 2 hour orbit. One could characterize the aerobraking orbits into three types of orbit regimes: large, medium, and small. A robust IMU navigation tool should be able to perform well in all three aerobraking regimes. Thus, data from orbits with periods near 16 (P-22)^{§§§§§§}, 6 (P-104), and 2 (P-329) hours were analyzed using IMAN.

The IMU data obtained from the spacecraft team at Lockheed Martin was adjusted in the following way:

^{§§§§§§} This nomenclature refers to the orbit after the numbered periapsis (i.e., P-22 refers to orbit after periapsis 22). For Mars Odyssey, P-1 occurred during the Mars Orbit Insertion burn.

1. Corrected for rollover (§III.A)
2. Converted from IMU case frame to the spacecraft body frame
3. Converted into engineering units: velocities and angles
4. Corrected for biases
5. Converted to accelerations and angular rates
6. Corrected for accelerometer-sensed centripetal acceleration

Figure 2 illustrates the Mars Odyssey aerobreaking configuration. The IMU measurements begin well before and after the drag pass, in a region where the output should be null. This allows for the identification of the bias (and its subsequent removal from the measured acceleration). Since the IMU is not located at the spacecraft center-of-mass, any angular motion will induce a centripetal acceleration sensed by the accelerometers. This acceleration is also removed from the signal.

The simulated data analysis indicated that there was little value in fitting IMU data in orbital regimes above 130 kilometers in altitude. It is worth noting that this might not be the case with a more sensitive IMU, such as one that could measure accelerations on the order of solar radiation pressure. Given the Odyssey IMU measurement accuracy, the IMU data used were truncated to that within 130 kilometers from the surface. Both the epoch state and its associated full covariance were mapped forward to the appropriate time, coinciding with this “truncated” IMU data set. This epoch state and covariance were then loaded into the IMAN MATLAB routine. Another file obtained from the archived Odyssey aerobreaking data set was the associated Small Forces (Small Accelerations [SFF]) file. This file contains data associated with spacecraft center of gravity (CG) ΔV increments and burn durations (Δt) in J2000 coordinates resulting from thruster firing events. The SFF file also contains an associated inertial-to-body spacecraft attitude quaternion, for each thrusting event. The parsed SFF file was loaded into IMAN and at the appropriate event end-times the information was applied to the spacecraft position and velocity states as follows.

AEROBRAKING CONFIG - NORMAL

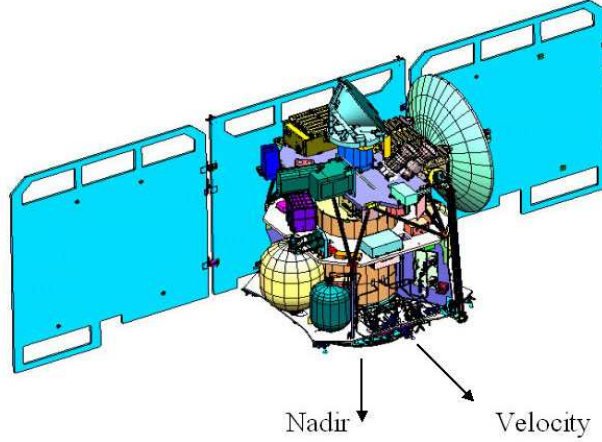


Figure 2. Mars Odyssey normal aerobreaking configuration¹⁶. Spacecraft Axes: +Z (radial or anti-nadir), +X (cross-track), +Y (anti-intrack or anti-velocity).

$$\mathbf{X}_{updated} = \mathbf{X}_{current} + \Delta \mathbf{X} = \begin{bmatrix} x + \frac{1}{2} \Delta V_x \Delta t \\ y + \frac{1}{2} \Delta V_y \Delta t \\ z + \frac{1}{2} \Delta V_z \Delta t \\ \dot{x} + \Delta V_x \\ \dot{y} + \Delta V_y \\ \dot{z} + \Delta V_z \end{bmatrix} \quad (14)$$

In the MATLAB routine, the current-time numerically integrated quaternion was replaced by the quaternion on the SFF file. Every aerobreaking orbit had an associated SFF file. One of the main reasons for these drag pass thruster firings was the desaturation of the RWA. A “free” AMD can be achieved in two of the three spacecraft axes. Aerodynamic forces keep the spacecraft stable in pitch and yaw, and these forces are strong enough to allow for the commanded despining of the reaction wheels without imparting angular motion to the spacecraft. Since this is not necessarily true for the roll axis, this axis is typically desaturated by the use of the RCS thrusters.

A. Large orbits (P-22)

An orbit representative of a large orbit is P-22, with roughly a 16 hour period. The duration of the effective drag pass for this orbit is on the order of 350 seconds, which is fairly short compared to the smaller orbits (~ 2 hour period) whose drag pass durations are on the order of 1000 seconds. It should be noted that the amount of ΔV removed from every orbit is approximately the same. This is by design, since the dynamic pressure corridor constraints are fairly constant throughout aerobraking *****.

Navigation is primarily interested in the overall effect of drag on the orbit, which is not a driver for improving the atmosphere model so long as the next periapsis time can be predicted to within the 225 second constraint. However, with an increasing demand for better navigation through low Mars orbits, there is a great benefit to improving our understanding of Mars atmospheric behavior. This motivates the real time reconstruction of the atmosphere, and is a benefit from processing IMU data collected throughout the drag pass. Figure 3 shows the reconstructed density profile, from the IMU data fit, for P22. The filtering strategy used for the results shown was the UKF, a specific form of the more commonly known sigma-point filter^{17, 18}. The results obtained by the EKF are very similar, and showing them would be redundant.

Inbound and outbound, in Fig. 3, refer to the path in and out of the atmosphere that was negotiated by the spacecraft. What is interesting about this plot is the structure that can be seen in the density near periapsis. This structure is real¹⁹. The Mars Odyssey Atmospheric Advisory Group (which included Ref. 19), theorized that a polar vortex existed at the Mars north pole, and that this phenomena, affecting the local density, was visible in the IMU data. This group also held that there were longitude dependent density waves and that density variation near periapsis could be up to 40% within a few seconds.

The advantage in reconstructing the density with this filtering technique versus matching IMU data with the navigation trajectory is that the navigation trajectory has no data through the atmosphere so it cannot reflect the real-

time changes that take place in the atmosphere. The navigation trajectory is the best estimated fit based on data before and after the drag pass, not during the drag pass. This is where processing IMU data as a navigation measurement and fitting a trajectory to this data in real-time (or in a current state filter), allows for a more realistic atmospheric structure to be recovered. This in turn, in the hands of atmospheric scientists, becomes the information needed in order to produce realistic improvements to current atmosphere models. In order to quantify how well the density can be recovered and at what altitudes is this density practically immeasurable, Figure 4 shows the reconstructed density Signal-to Noise Ratio (SNR) for P22. The method by which the SNR is computed (at each time step) follows. First, we rotate the MCI-frame **RMS** to the RIC-frame.

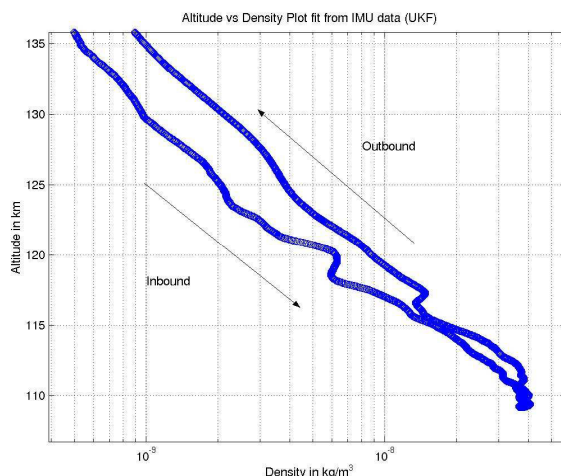


Figure 3. Altitude vs. density profile reconstructed from IMU data fit for P22 using the UKF

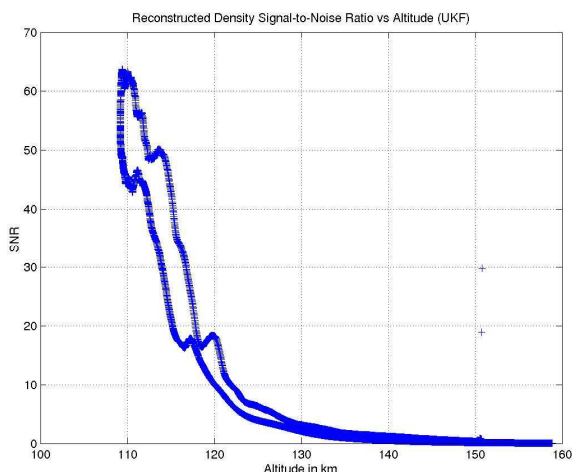


Figure 4. Reconstructed density signal-to-noise ratio (SNR) for P22 (UKF)

***** Neglecting end-game which has an orbit lifetime constraint based on the integrated heating effect rather than a fixed heating rate limit which maps to a dynamic pressure limit.

$$\mathbf{RMS}_{RIC} = \mathbf{T}_{RIC}^{MCI} \mathbf{RMS}_{MCI}$$

Since the density is based upon the drag accelerations, we use the intrack **RMS** value. We scale this by three in order to get a SNR of one for a density reconstructed value that is right at the 99% threshold of all noise values.

$$a_{noise} = 3 \mathbf{RMS}_I$$

Then, for this equivalent acceleration due to drag, we compute the density value.

$$\rho_{noise} = -\frac{2 a_{noise} m}{|\bar{\mathbf{V}}|^2 C_d A} \quad (15)$$

Finally, SNR is computed by taking the reconstructed density and dividing it by Eqn 15.

$$SNR = \frac{\rho_{reconstructed}}{\rho_{noise}} \quad (16)$$

As can be seen from Fig. 4, the SNR is fairly close to zero around 150 kilometers in altitude. It is not until around 135 kilometers from the surface, that the SNR becomes larger than 2. This implies that confidence in density estimates above this altitude should be very low, since the signal is in the noise. Alternatively, it is interesting to note that the structure seen in the density reconstruction is very observable from a SNR perspective. To understand the relative magnitudes of the drag-pass accelerations and body rates, they are plotted in Fig. 5 and Fig.6

Drag is by far the dominant non-conservative force acting upon the spacecraft. As shown in Fig. 7, the nominal drag-pass attitude aligns the spacecraft –Y-body axis along the spacecraft velocity vector. This attitude is not exactly maintained during the drag pass, as can be seen from the attitude oscillations that the spacecraft experiences shown in Fig. 6. Therefore, there is some drag effect that is experienced along the other spacecraft body axes. This is reflected in the accelerometer data. It is worthwhile noting that due to these attitude oscillations, there are also lift and side-forces experienced by the spacecraft.

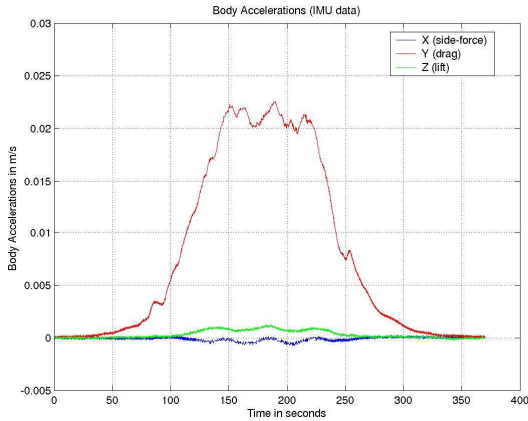


Figure 5. Accelerometer data expressed in the spacecraft body frame for orbit P22.

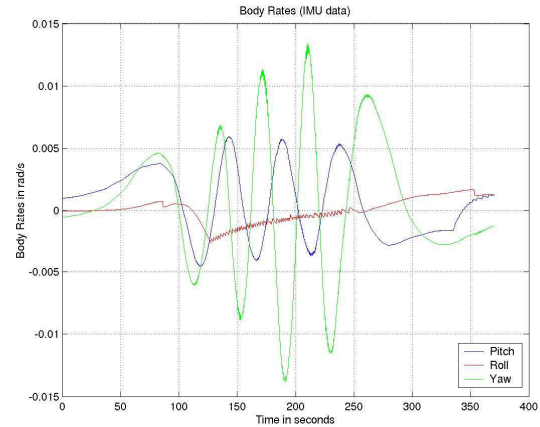


Figure 6. Gyroscope data expressed in the spacecraft body frame for orbit P22.

The spacecraft pitched and yawed throughout the drag pass. This profile is typical of all aerobraking orbits. Aerodynamic torques keep the spacecraft mostly drag-pointed. Typical angle offsets from nominal are between 10 to 15 degrees. The discontinuities observed in the roll axis are the effect of the thruster firings, desaturating the RWA. Figures 7 and 8 show the observation residuals (the difference between the observed accelerations from the IMU versus the filter estimate of what those accelerations should be) for P22, expressed in the radial-intrack-crosstrack frame.

Since the innovations standard deviation is an order of magnitude larger than the residuals themselves (making

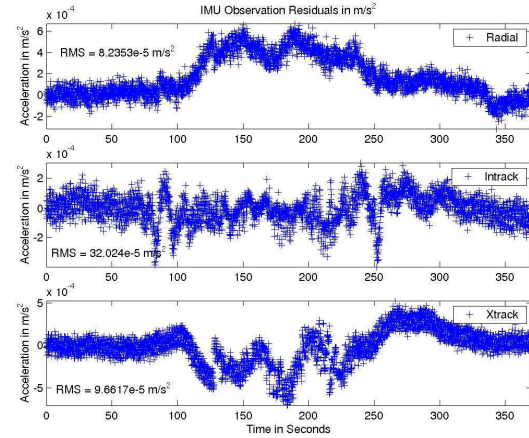
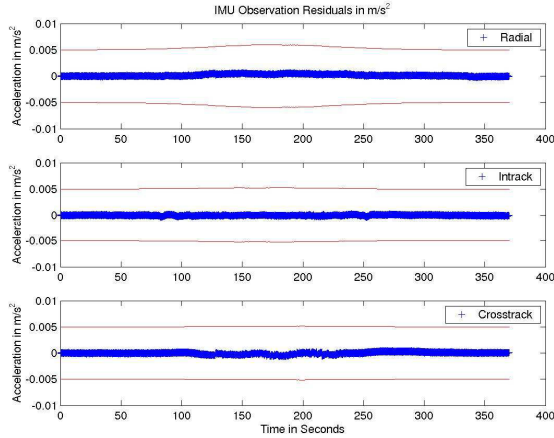


Figure 7. IMU observation residuals for P22 on a bounded by the innovations standard deviation reduced scale (UKF)
the residuals appear to be white) the residuals are zoomed in to reveal their true structure, in Fig 8. In order to directly compare the observations to the computed values, Figs. 9 through 11 show the observed versus computed quantities in the radial, intrack, and crosstrack directions.

The discontinuities observed in Fig. 9 are the products of nearly 50 thrusters firing attitude updates that occurred during the P22 drag pass. The lift and sideforce are not being modeled explicitly. Although they are very small compared to the drag force, this still produces some level of mismodeling. Another point to note is that the thruster firings are assumed to be perfectly known in this analysis. In reality, there is some level of error in the thruster pulses themselves and the information given to the navigation team within the small forces file may be biased. Typically, the navigation team estimated a stochastic scale factor, applied to the small force data, in order to account for these errors. This scale factor is not being estimated here and is a potential source of improvement of these results.

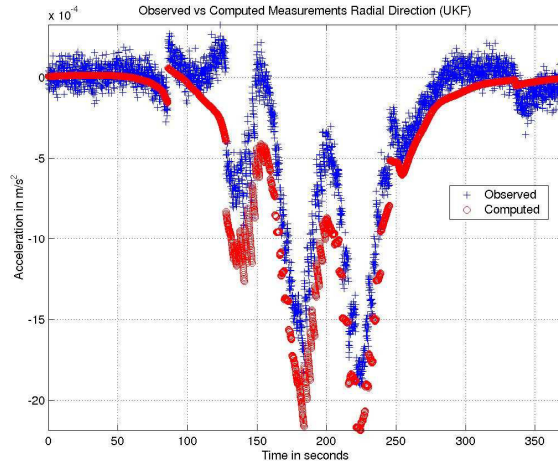


Figure 9. Observed versus computed non-gravitational accelerations in the radial direction for P22 (UKF).

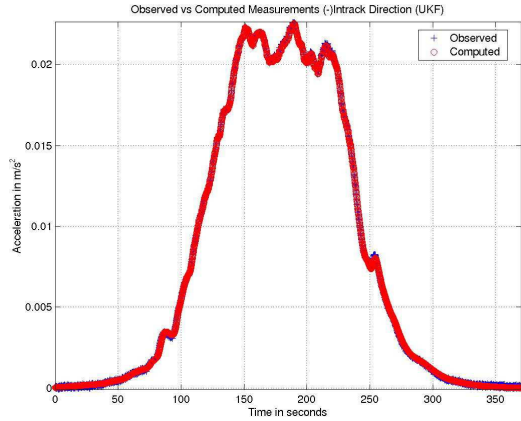


Figure 10. Observed versus computed non-gravitational accelerations in the radial direction for P22 (UKF)

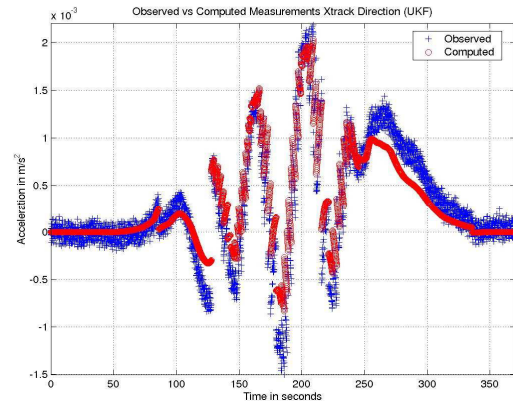


Figure 11. Observed versus computed non-gravitational accelerations in the crosstrack direction for P22 (UKF).

Figure 10 shows the drag pulse for P22. As can be seen, the observed and computed quantities lay on top of each other. The structure seen in this figure reflects true variations in the Mars atmosphere during the drag pass. Interesting to note are the two “humps” entering and leaving the atmosphere. Atmospheric scientists theorized that there was a “polar vortex” evident in the data around these early orbits since periapsis is naturally precessed through the planets north pole due to oblateness effects at this time^{††††††††}.¹⁹. The filter performs acceptably in fitting the drag pulse. Again, Fig. 11 shows the effects of the thruster pulse attitude updates upon the data. Overall, the filter performs reasonably well in fitting the IMU data in the crosstrack direction. Figure 12 shows the 3σ error ellipsoid in the radial-intrack-crosstrack coordinate frame, at the end of the drag-pass^{#####}.

A covariance study was performed in order to assess the size and orientation of the unfiltered state uncertainties following the drag pass. This result reflects the expected covariance, given no knowledge of the drag-pass dynamics. The result from this covariance study is plotted along with the resultant error ellipse obtained from IMAN (using the UKF), and is provided in Fig. 13. In essence, the results show the difference between the state uncertainties knowing nothing about the drag-pass and just having measured it with the IMU.

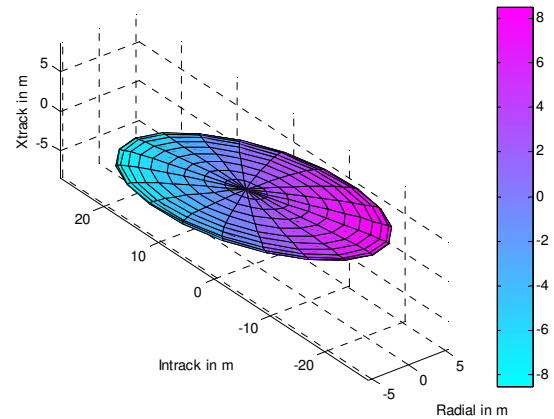


Figure 12. 3σ error ellipsoid in radial-intrack-crosstrack coordinates for P22 (UKF)

^{††††††††} Personal communication with Richard Zurek (2005).

^{#####} For clarity, the error ellipsoid is plotted without the mean (or bias), therefore strictly showing uncertainties about the mean. Subsequent error ellipsoid plots are similar.

As can be seen from Fig 13, the IMAN ellipse is well within the covariance study ellipse. To illustrate the relative IMAN ellipse size, Fig. 14 shows the previous result on a reduced scale.

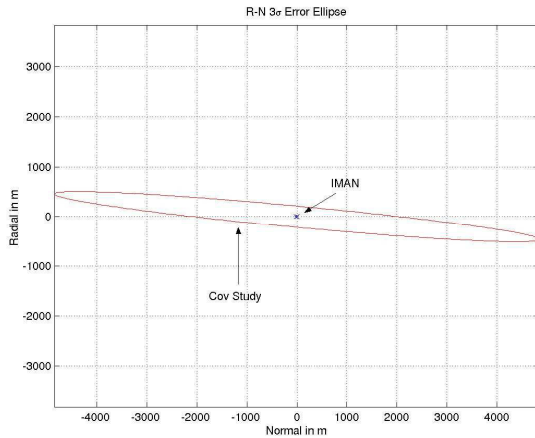


Figure 13. Radial-normal (crosstrack) plane covariance study versus IMAN 3σ error ellipse comparison for P022

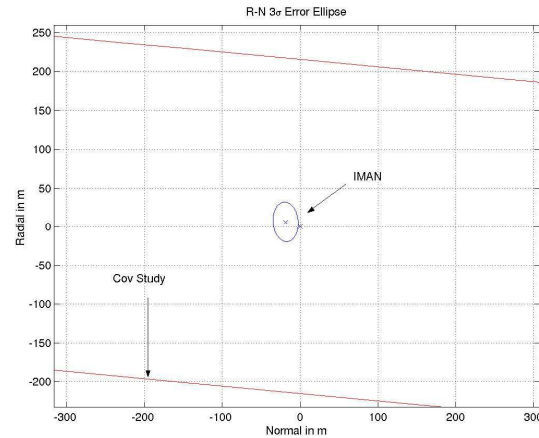


Figure 14. Reduced scale radial-normal plane covariance study versus IMAN 3σ error ellipse comparison for P022

To get a more qualitative idea of how well IMAN performed, Fig. 15 shows the 3σ error ellipsoids between the post drag pass navigation team solution and IMAN projected upon the plane nearly normal to the velocity vector (direction of motion). These error ellipses have their epoch at the end of the drag pass. The navigation (NAV) ellipse is based upon radiometric data processed both before and after the drag pass, and represents NAV's best estimate of the state uncertainties mapped to the post-drag pass epoch. The IMAN ellipse is based upon information collected prior to and during the drag-pass. The IMAN solution has no knowledge of the radiometric data after the drag pass. To clarify, the IMAN solution is what one would get as soon as the drag pass finished. The NAV solution is what one would get by waiting for approximately one hours worth of Doppler data following the drag pass, fitting it, and mapping that solution back to the IMAN post-drag pass epoch.

The IMAN solution is consistent with the NAV solution. It is well worth noting that these errors are only at the post-drag pass epoch. As the spacecraft spends more time in the vacuum regime of the orbit, and more Doppler data are collected and fit, these NAV errors become greatly reduced, whereas the IMAN solution uncertainties will begin to grow in the absence of more observations.

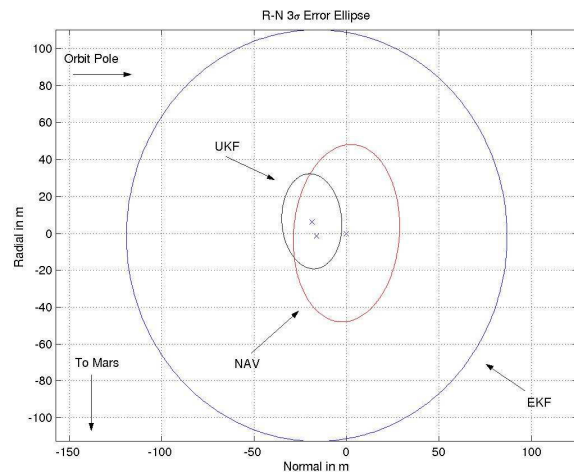


Figure 15. Radial-normal plane 3σ error ellipses for P22

Figures 16 and 17 show the 1σ current state uncertainties (position and velocity) expressed in the radial, intrack, and crosstrack directions.

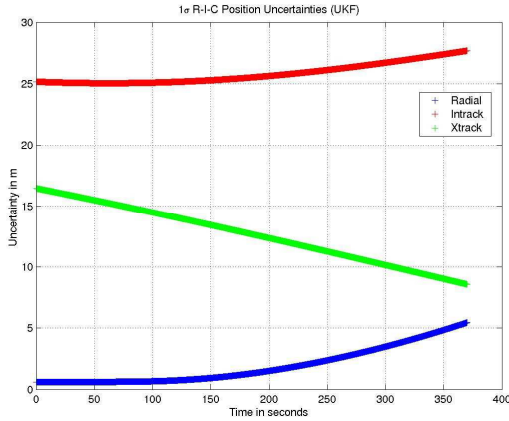


Figure 16. Radial, intrack, and crosstrack position current state errors for P22

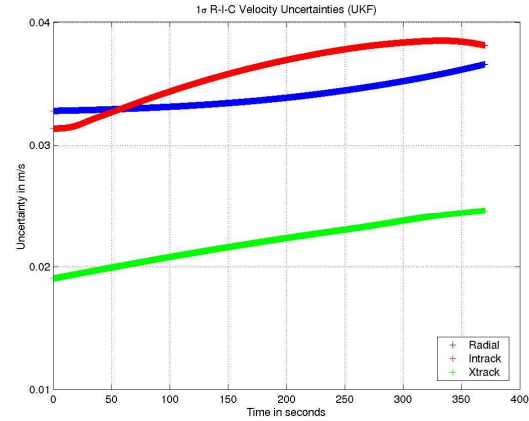


Figure 17. Radial, intrack, and crosstrack velocity current state errors for P22

Given the previous figures, it can be seen that the state uncertainties (having already started out as being relatively small), are not significantly reduced but they are constrained in their growth. The covariance is realistic. Later orbits (smaller orbits) typically have larger *a priori* covariances due to the fact that the spacecraft spends less time in the vacuum regime, and thus less Doppler data are fit for a given orbit. IMAN is sensitive to this larger covariance^{§§§§§§}, as shall be shown subsequently. Eventually, the velocity errors dominate and IMAN does a less successful job in recovering the out of plane drag pass dynamics. The states from the various filter strategies are differenced from the UKF and compared to the final NAV solution. Figures 18 and 19 show these Cartesian coordinate position and velocity state differences.

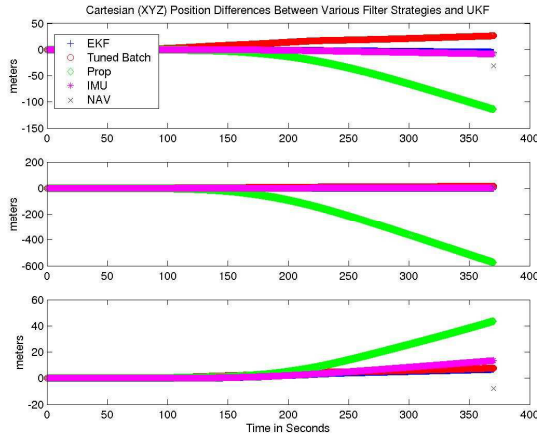


Figure 18. Cartesian position differences (in meters) between various filter strategies and the UKF solution for P22

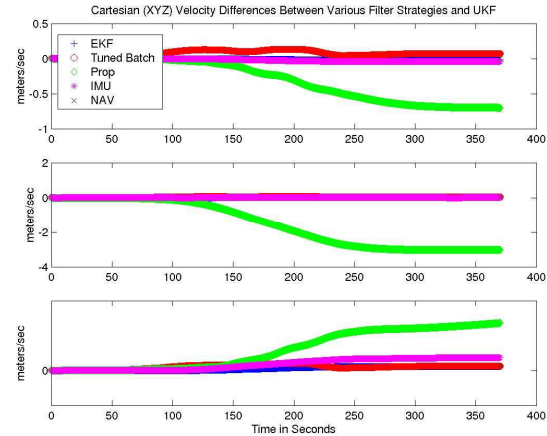


Figure 19. Cartesian velocity differences (in meters per second) between various filter strategies and the UKF solution for P22

The previous figures are generated by subtracting the various states from the UKF states. In that sense, the comparison is truly against the UKF results. The results labeled “Prop” are achieved by simply propagating the state with the *a priori* atmosphere model. It is shown that this method yields inaccurate results due to the error in the atmosphere model. The results labeled “IMU” are achieved by not using a filter, but rather using the IMU in lieu of an atmosphere model. It is the result of propagating a state and replacing the atmospheric acceleration equations with the direct accelerometer measurements. The IMU propagated state produces an acceptably accurate result since

^{§§§§§§} Fairly large position errors can be tolerated by IMAN; The IMAN sensitivity is primarily to velocity errors.

the IMU is a direct measure of the true atmospheric dynamics. The IMU propagated results are commensurate with the filter results because the IMU data is the best information available about the atmosphere; the filter has a poor atmosphere model and relies on the IMU data to inform it of the real atmosphere. The IMU propagation solely relies on the IMU data as the atmosphere model. Both methods rely on the IMU data to know what the atmosphere is.

Figures 18 and 19 demonstrate that it is better to use the IMU data than to not use it at all. However, filtering the IMU data provides additional benefits over simply propagating the trajectory with the IMU as the atmosphere model. These benefits include: (a) having a realistic associated uncertainty along with the state, based upon the IMU data, (b) obtaining density reconstruction estimates for use for possible model atmospheric model improvement, and (c) having a method that would still have an atmospheric model in the event of an IMU data outage.

To conclude the results for these larger aerobraking orbits, Tables 2 through 4 show the performance of the various filter strategies against the NAV solution^{*****}. A brief description of relevant parameters on the Differenced State file is provided in Table 1. These differences are reflected at a fixed time.

Table 1. Differenced State file parameter description

Description	Parameter Name
Earth-Mean-Equator of 2000 Position and Velocity	X,Y,Z,DX,DY,DZ
Absolute Position Difference	lposl
Absolute Velocity Difference	lvell
Semi-major Axis	SMA
Eccentricity	ECC
Inclination	INC
Argument of Perifocus	APF
Longitude of Ascending Node	LAN
Time From Periapse Passage	TFP
Energy	C3
Period	PRD
Radius of Closest Approach	RCA
Radial position component in R-I-C frame	V1Rad
Intrack position component in R-I-C frame	V1DTrk
Crosstrack position component in R-I-C frame	V1Nrml
Radial velocity component in R-I-C frame	V1RadD
Intrack velocity component in R-I-C frame	V1DTrkD
Crosstrack velocity component in R-I-C frame	V1NrmlD

***** The JPL navigation team uses a tool called DIZZY, which differences states and provides this in a summary format.

As can be seen from Table 2, the batch does an acceptable job, yet not as good as the EKF and UKF which compare very well with each other. This is to be expected from the batch, since the drag pass non-linearities are captured better by the current state filters and the direct inclusion of the IMU data as part of the dynamic model.

Table 2. NAV vs. IMAN solution comparison for P22

Paramter	NAV-IMU	NAV-Batch	NAV-EKF
lposl (KM)	0.031	0.060	0.030
lvell (CM/S)	6.664	7.686	3.231
SMA (KM)	-1.230	4.017	-1.365
PRD (HMS)	-00:00:06.96	-00:00:22.73	-00:00:07.72
V1Rad (KM)	-0.008	0.017	-0.001
V1DTrk (KM)	0.028	0.055	0.026
V1Nrml (KM)	-0.012	-0.017	-0.016
V1RadD (CM/S)	-6.556	4.066	-1.625
V1DTrkD (CM/S)	-1.066	6.096	-2.376
V1NrmlD (CM/S)	-0.543	-2.317	-1.468

Another measure of how well IMAN performed can be found in comparing the maximum dynamic pressures and heat rates. These two parameters are the key to aerobraking corridor control strategies and operations. Violating either side of the corridor will incite an action from the operations team. Not experiencing enough drag may prompt a periapsis lowering maneuver. The less benign side, experiencing too much drag, will prompt a periapsis raising maneuver. The ability of IMAN to satisfactorily detect the maximum heating rate and dynamic pressure is crucial if it is to be relied upon during aerobraking operations. Table 3 shows the comparison between the NAV and IMAN reconstructed values of these parameters.

Table 3. Maximum dynamic pressure and heat rate comparison between NAV and IMAN for P22 (UKF)

Drag Pass Parameter	NAV	IMAN
q_{\max} (N/m ²)	0.466	0.443
\dot{q}_{\max} (W/cm ²)	0.218	0.207

IMAN is able to detect these quantities to within 5% of the navigation team solution. In fact, it may be arguable that IMAN is more correct, given that the IMU directly measures the dynamics which determine these parameters.

Figure 20 shows results from the Odyssey Atmospheric Advisory Group (AAG) for P22. Quantitatively, it compares well with the IMAN results (Fig 3). Qualitatively, IMAN shows higher resolution of the density structure. This, in part, is due to the fact that the AAG solution is using 39 second-averaged data, whereas IMAN fits IMU data at 10 Hz.

Finally, a comparison in the ability to predict the subsequent periapsis time and altitude between NAV and IMAN can be seen in Table 4. There is no formal requirement for periapsis altitude prediction while the timing requirement is 225 seconds. However, predicted density values are highly correlated with periapsis altitude predictability.

IMAN is within several seconds and meters from the NAV values. It is shown that there is no need for post-drag pass radiometric data to successfully determine subsequent periapsis quantities, if implementing IMAN. It must be noted that IMAN would eventually need to be reinitialized with an updated radiometric solution as errors would accumulate in time and reach a point where IMAN is likely to be unable to recover state errors. Determining how long IMAN could be relied upon without being reinitialized with a radiometric solution (i.e., use the same *a priori* state and associated covariance for multiple orbit revolutions), will be pursued with current follow-on funding.

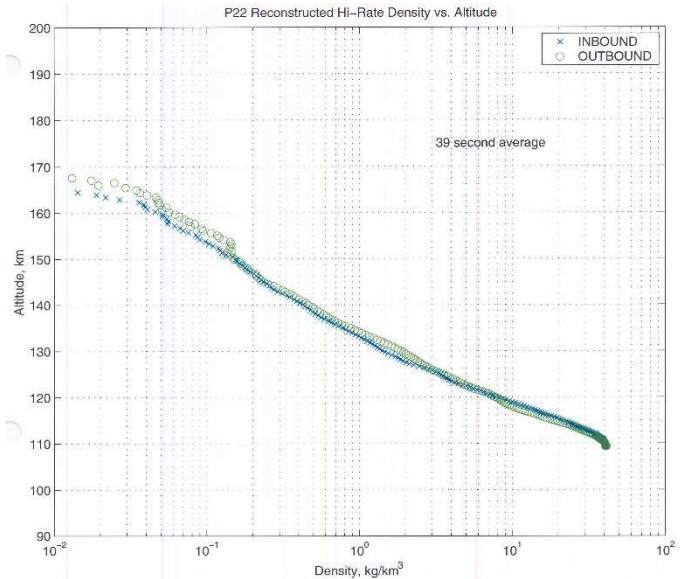


Figure 20. Accelerometer Advisory Group (AAG) Reconstructed Density Profile (P22) (Zurek, 2005)

Table 4. NAV vs. IMAN subsequent periapsis condition comparison for P22 (UKF)

Subsequent Periapsis Stats	Timing (sec)	Altitude (m)
NAV Predicted-IMAN	-5.124	-3.653
NAV Reconstructed-IMAN	-4.976	-4.351
NAV Predicted-NAV Reconstructed	0.148	-0.697

The performance achieved from processing IMU data during medium and smaller sized orbits is similar to that shown for the larger orbit (P22). Therefore what follows are tables summarizing this performance for the two other orbit regimes.

B. Medium Orbits (P-104)

Table 5 shows the performance of the various filter strategies against the NAV solution for P104. Note that, consistent with the *a priori* state uncertainties, the largest deviations from the navigation solution are in-track position and radial velocity.

Table 5. NAV vs. IMAN solution comparison for P104

Paramter	NAV-IMU	NAV-Batch	NAV-EKF	NAV-UKF
lposl (KM)	0.170	0.157	0.167	0.170
lvell (CM/S)	32.704	70.065	28.966	24.638
SMA (KM)	-0.253	-7.812	-0.314	0.047
PRD (HMS)	-00:00:01.02	-00:00:32.42	-00:00:01.27	00:00:00.19
V1Rad (KM)	-0.016	0.004	-0.016	-0.006
V1DTrk (KM)	0.169	0.157	0.166	0.170
V1Nrml (KM)	0.008	0.003	-0.002	-0.008
V1RadD (CM/S)	-28.055	-33.434	-26.121	-22.548
V1DTrkD (CM/S)	2.310	-59.434	1.599	3.226
V1NrmlD (CM/S)	16.647	16.091	12.415	9.393

The batch does an acceptable job, yet not as good as the EKF and UKF which compare very well with each other. Using the IMU as a replacement for the atmosphere model, yields better results commensurate with the UKF. These results are provided in Differenced State files seen in the previous figures. Another measure of how well IMAN performed can be found in comparing the maximum dynamic pressures and heat rates. Table 6 shows the comparison between the NAV and IMAN reconstructed values of these parameters.

Table 6. Maximum dynamic pressure and heat rate comparison between NAV and IMAN for P104 (UKF)

Drag Pass Parameter	NAV	IMAN	% Difference
q_{\max} (N/m ²)	0.733	0.631	13.9
\dot{q}_{\max} (W/cm ²)	0.323	0.277	14.2

Although IMAN is within 14% of the navigation team solution, this should not be alarming. There are orbits where the spacecraft team at Lockheed Martin had up to 300% differences with the navigation team. Again, it should be noted that IMAN directly measures the atmospheric dynamics which determine these parameters. Finally, a comparison in how well can the subsequent periapsis time and altitude are predicted follows.

Table 7. NAV vs. IMAN subsequent periapsis condition comparison for P104 (UKF)

Subsequent Periapsis Stats	Timing (sec)	Altitude (m)
NAV Predicted-IMAN	0.193	-1.348
NAV Reconstructed-IMAN	0.211	-1.267
NAV Predicted-NAV Reconstructed	0.017	0.082

IMAN is only within tenths of a second and just over a meter from the NAV values. It is shown that IMAN can successfully determine subsequent periapsis quantities.

C. Small Orbits (P-329)

Table 8 shows the performance of the various filter strategies against the NAV solution for the smaller orbit, P329.

Table 8. NAV vs. IMAN solution comparison for P329

Paramter	NAV-IMU	NAV-Batch	NAV-EKF	NAV-UKF
lposl (KM)	0.437	0.406	0.441	0.426
lvell (CM/S)	35.647	57.289	38.398	39.792
SMA (KM)	0.015	0.005	-0.003	0.053
PRD (HMS)	-00:00:00.04	00:00:00.01	-00:00:00.00	00:00:00.14
V1Rad (KM)	-0.110	0.094	-0.115	-0.104
V1DTrk (KM)	-0.422	-0.394	-0.426	-0.413
V1Nrml (KM)	0.032	0.018	0.009	0.006
V1RadD (CM/S)	24.085	49.413	24.596	25.639
V1DTrkD (CM/S)	10.542	-10.169	10.234	11.554
V1NrmlD (CM/S)	-24.072	-27.146	-27.653	-28.152

Although the batch has been shown to yield poorer results, it should be noted that the performance of the batch processor is in part levied upon the modeling capability employed by this strategy. Process noise can be incorporated in the current state filters, in a straightforward manner. This is not true for the batch. Table 9 shows the comparison between the NAV and IMAN reconstructed values of both the maximum dynamic pressure and heating rate for P329.

Table 9. Maximum dynamic pressure and heat rate comparison between NAV and IMAN for P329 (UKF)

Drag Pass Parameter	NAV	IMAN	% Difference
q_{\max} (N/m ²)	0.051	0.052	1.9
\dot{q}_{\max} (W/cm ²)	0.141	0.146	3.5

Once more, IMAN is able to detect these quantities to within a few percent of the navigation team solution.

The subsequent periapsis conditions comparison between NAV and IMAN follows in Table 10.

Table 10. NAV vs. IMAN subsequent periapsis condition comparison for P329 (UKF)

Subsequent Periapsis Stats	Timing (sec)	Altitude (m)
NAV Predicted-IMAN	1.050	9.200
NAV Reconstructed-IMAN	1.495	-3.856
NAV Predicted-NAV Reconstructed	0.389	13.058

IMAN shows that it can be relied upon for successfully determining these quantities. IMAN has performed satisfactorily across all orbit regimes.

V. Conclusions

The research clearly shows that filtering IMU data during aerobraking yields acceptable post drag-pass state estimates, consistent reconstructed density profiles, and subsequent periapsis time and location estimates. Propagating the spacecraft state, while using the IMU data in lieu of atmospheric dynamic equations, leads to acceptable results. However, there are benefits to filtering the IMU data instead. These benefits include: (a) having a realistic associated uncertainty along with the state, based upon the IMU data, (b) obtaining density reconstruction estimates for use for possible model atmospheric model improvement, and (c) having a method that is robust in the presence of an IMU data outage.

The results achieved by IMAN (which does not incorporate post-drag-pass data) are comparable to the navigation solution, which includes post-drag-pass radiometric data. This indicates that IMAN provides a reliable independent assessment of the drag-pass dynamics without the need for further radiometric data processing. Typically, the navigation team is allotted 3 hours past periapsis to collect and reduce radiometric data, and deliver trajectory products to engineering and science teams. IMAN achieves its results in an amount of time equivalent to the sensed drag-pass. This means that if the sensed drag pass duration was 350 seconds it would take 350 seconds for IMAN to produce drag-pass state estimates.

Spacecraft events, such as slewing to and from drag-pass attitudes, take place relative to the predicted periapsis times which are required to be within 225 seconds in error. Since periapsis altitude is highly correlated with atmospheric density, and thus the dynamic pressure experienced by the spacecraft, it is in the interest of the navigation team to minimize periapsis altitude uncertainties. This error is typically constrained to 1.5 kilometers⁷. The research shows that IMAN can be used to reliably predict subsequent periapsis times to within several seconds and locations to within several meters, over all aerobraking regimes.

During aerobraking, a dynamic pressure or heating rate corridor is defined so as to meet mission requirements and keep the spacecraft from potential burning up in the atmosphere. If the spacecraft violates the upper corridor limit (too high a heating rate), then a periapsis raising maneuver must be commanded and successfully implemented in order to insure mission safety. The research shows that IMAN also yields accurate peak dynamic pressure and heating rates, critical for a successful corridor control strategy, matching navigation team values to within several percent.

A cornerstone of aerobraking operations is the participation of the Atmospheric Advisory Group (AAG), comprised of expert interplanetary atmospheric scientists. These experts attempt to characterize the atmosphere on a daily basis, with the intent of refining current atmospheric models. IMAN is shown to produce consistent, reconstructed density profiles^{††††††††}, as compared to AAG results archived during the Mars Odyssey aerobraking phase. The IMAN density reconstructions have a greater resolution than previously achieved by the AAG. This is because of the fact that accelerometer measurements collected by the AAG were coupled to spacecraft states based on the navigation solution, which was a least squares fit through the drag-pass. IMAN, being a current state filter, produces state estimates achieved by fitting the accelerometer data and yields reconstructed density values at each measurement. Therefore, the density profile has a resolution equivalent to the measurement time span, in this case at every 0.1 seconds.

^{††††††††} Personal communication with Richard Zurek (2005).

This research provides the first instance of the utilization of the UKF for the purpose of estimating an actual spacecraft trajectory arc about another planet. The UKF produced consistent results across the various orbit regimes, and delivered realistic covariances. It must be noted that although the results obtained from a specific orbit may be improved with fine tuning, the research proved that a robust filter strategy can be successfully employed, since the filter parameters were maintained constant across all aerobraking regimes, yielding acceptable results.

Acknowledgments

The work described in this paper was carried out at the Jet Propulsion Laboratory, California Institute of Technology, under a contract with the National Aeronautics and Space Administration. Reference herein to any specific commercial product, process, or service by trade name, trademark, manufacturer, or otherwise, does not constitute or imply its endorsement by the United States Government or the Jet Propulsion Laboratory, California Institute of Technology.

The authors acknowledge the assistance of those individuals who made this research possible: Dan Lyons, whose initial funding helped get this research underway; Joe Guinn, who helped with the conception of this research topic; Dolan Highsmith, who was used relentlessly as a sounding board for this research; Tung-Han You, whose insight and grasp of the problem served as a well calibrated set of independent eyes that assisted in seeing solutions to the problem; Dan Burkhart, for taking time away from more important tasks in order to review this body of work; and Jay Wyatt for channeling the funding necessary to see this research through to a meaningful end. Moriba Jah gives special thanks to Michael Lisano, George Born, and Penina Axelrad for their sound advice, guidance, and support; their contributions to this research proved to be of immeasurable value.

References

- ¹Jah, M.K., "A Proposed Use of Accelerometer Data for Autonomous Aerobraking at Mars," *AIAA/AAS Astrodynamics Specialist Conference*, AAS 01-386, Quebec City, Canada, 2001, July 30 – August 2.
- ²Jah, M.K., Lisano, M.E. II, "6-DOF Aerobraking Trajectory Reconstruction by use of Inertial Measurement Unit (IMU) Data for the Improvement of Aerobraking Navigation," *14th Space Flight Mechanics Meeting*, AAS 04-214, Maui, HI., 2004, February 8-12.
- ³NASA Space Vehicle Design Criteria (Guidance and Control). "Space Vehicle Accelerometer Applications," NASA SP-8102., 1972.
- ⁴Blanchard, R.C., Larman, K.T., and Barrett, M., "The High Resolution Accelerometer Package (HiRAP) Flight Experiment Summary for the First 10 Flights," NASA RP-1267, 1992.
- ⁵Bishop, R., Dubois-Matra, O., "Development of a Planetary Entry Model Suitable for Processing Acceleration Measurement," Interim Report #1 to Todd Ely (JPL), 2001.
- ⁶Wawrzyniak, G., Lisano, M., "Using Inertial Measurements for the Reconstruction of 6-DOF Entry, Descent, and Landing Trajectory and Attitude Profiles," *AIAA/AAS Astrodynamics Specialist Conference*, AAS 02-164, San Antonio, TX, 2002, January 27-30.
- ⁷Willcockson, W., Johnson, M., "Mars Odyssey Aerobraking: The First Step Toward Autonomous Aerobraking Operations," *Proceeding of 2003 IEEE Aerospace Conference*, Vol. 8, Big Sky, MT, 2003, pp. 3503-3510.
- ⁸Lyons, D.T., Sjogren, W., Johnson, W., Schmitt, D., McDonald, A., "Aerobraking Magellan," *AIAA/AAS Astrodynamics Specialist Conference*, AAS 91-420, Durango, CO., 1991, August 19-22.
- ⁹Wong, S.K., You, T-H., Giorgini, J.D., Lim, L., Chadbourne, P., "Navigating Through the Venus Atmosphere," *AIAA/AAS Astrodynamics Specialist Conference*, AAS 94-116, Cocoa Beach, FL., 1994, February 14-16.
- ¹⁰Esposito, P., Alwar, V., Demcak, S., Graat, E., Johnston, M., Mase, R.A., "Mars Global Surveyor: Navigation and Aerobraking at Mars," *AIAA/AAS Astrodynamics Specialist Conference*, AAS 98-384, Monterey, CA., 1998, February 9-11.
- ¹¹Smith, J., Bell, J., "2001 Mars Odyssey Aerobraking," *AIAA/AAS Specialist Conference*, AIAA 2002-4532, Monterey, CA., 2001, August 5-8.
- ¹²McDonald, A., "Use of Atmospheric Drag to Circularize an Elliptic Spacecraft Orbit at Venus," JPL 760-163, 1977.
- ¹³Mase, R., Antreasian, P., Bell, J., Martin-Mur, T. (2002, August 5-8). The Mars Odyssey Navigation Experience, AIAA 2002-4530, AIAA/AAS Astrodynamics Specialist Conference, Monterey, CA.
- ¹⁴Honeywell Inertial Sensor Products, <http://www.inertialsensor.com>, [cited 15 April 2005].
- ¹⁵Cancro, G.J, Tolson, R.H., and Keating, G.M. (1998). *Operational Data Reduction Procedure for Determining Density and Vertical Structure of the Martian Upper Atmosphere from Mars Global Surveyor Accelerometer Measurements*. NASA/CR-1998-208721.
- ¹⁶Mase, R.A. (2001). *2001 Mars Odyssey: Navigation Plan and Trajectory Characteristics; Final Version*. JPL D-16001 722-202.

¹⁷Julier, S.J., Uhlmann, J.K., "A New Extension of the Kalman Filter to Nonlinear Systems," *Proceedings of SPIE - The International Society for Optical Engineering*, Vol. 3068, Orlando, FL., 1997, April 21-24, pp. 182-193.

¹⁸van der Merwe, R., Wan, E.A., "The Square Root Unscented Kalman Filter for State and Parameter-Estimation," *2001 IEEE International Conference on Acoustics, Speech, and Signal Processing*. Vol. 6, Salt Lake City, UT., 2001, May 7-11, pp. 3461-3464.

¹⁹Tolson, R.H., Keating, G.M., George, B.E., Escalera, P.E., Werner, M.R., Dwyer, A., Hanna, J., "Application of Data to Mars Odyssey Aerobraking and Atmospheric Modeling," *AIAA/AAS Astrodynamics Specialist Conference*, AIAA-2002-4533, Monterey, CA (Accepted for publication in *Journal of Spacecraft and Rockets*), 2002, August 5-8.